

Quasi-Two-Dimensional Antiferromagnetic Spin Fluctuations in the Spin-Triplet Superconductor Candidate CeRh_2As_2

Tong Chen,^{1,*} Hasan Siddiquee,² Qiaozhi Xu,² Zack Rehfuss,² Shiyuan Gao,¹ Chris Lygouras,¹ Jack Drouin,¹ Vincent Morano,¹ Keenan E. Avers,³ Christopher J. Schmitt,⁴ Andrey Podlesnyak,⁴ Johnpierre Paglione,³ Sheng Ran,^{2,†} Yu Song,^{5,‡} and Collin Broholm^{1,6,§}

¹*Institute for Quantum Matter and Department of Physics and Astronomy,
Johns Hopkins University, Baltimore, Maryland 21218, USA*

²*Department of Physics, Washington University in St. Louis, St. Louis, Missouri 63130, USA*

³*Maryland Quantum Materials Center and Department of Physics,
University of Maryland, College Park, Maryland 20742, USA*

⁴*Neutron Scattering Division, Oak Ridge National Laboratory, Oak Ridge, Tennessee 37831, USA*

⁵*Center for Correlated Matter and School of Physics, Zhejiang University, Hangzhou 310058, China*

⁶*Department of Materials Science and Engineering,
The Johns Hopkins University, Baltimore, Maryland 21218, USA*

(Dated: December 11, 2024)

The tetragonal heavy-fermion superconductor CeRh_2As_2 ($T_c = 0.3$ K) exhibits an exceptionally high critical field of 14 T for $\mathbf{B} \parallel \mathbf{c}$. It undergoes a field-driven first-order phase transition between superconducting states, potentially transitioning from spin-singlet to spin-triplet superconductivity. To further understand these superconducting states and the role of magnetism, we probe spin fluctuations in CeRh_2As_2 using neutron scattering. We find dynamic (π, π) antiferromagnetic (AFM) spin correlations with an anisotropic quasi-two-dimensional correlation volume. Our data place an upper limit of $0.31 \mu_B$ on the staggered magnetization of corresponding Néel orders at $T = 0.08$ K. Density functional theory calculations, treating Ce $4f$ electrons as core states, show that the AFM wave vector connects significant areas of the Fermi surface. Our findings indicate that the dominant excitations in CeRh_2As_2 for $\hbar\omega < 1.2$ meV are magnetic and suggest that superconductivity in CeRh_2As_2 is mediated by AFM spin fluctuations associated with a proximate quantum critical point.

While phonon-mediated superconductivity is typically incompatible with magnetism, antiferromagnetic (AFM) spin fluctuations can promote unconventional superconductivity [1, 2] in various systems, including cuprates [3–6], Fe-pnictides [7–9] and chalcogenides [10, 11], and heavy-fermion metals [12]. Experimental evidence for magnetically driven superconductivity includes (i) spin resonance modes in the superconducting (SC) state [13–15], and (ii) paramagnetic excitations in the normal state with energies well beyond the SC gap [16–20]. Despite extensive efforts to understand the spin dynamics of spin-singlet unconventional superconductors, research on spin-triplet superconductors has been constrained by the scarcity of model systems [15, 21].

CeRh_2As_2 is a heavy-fermion superconductor with $T_c = 0.3$ K [22]. It adopts the tetragonal CaBe_2Ge_2 -type structure (space group No. 129 P4/nmm), consisting of two-dimensional (2D) Ce layers stacked with As-Rh-As and Rh-As-Rh blocks along the \mathbf{c} axis [Fig. 1(a) inset]. While the overall crystal structure is centrosymmetric, Ce layers are positioned between distinct blocks, leading to local inversion symmetry breaking and alternating Rashba spin-orbit coupling (SOC) [23, 24]. For $\mathbf{B} \parallel \mathbf{c}$,

CeRh_2As_2 exhibits pronounced anomalies in alternating current susceptibility, magnetization, and magnetostriction [22, 25–30], indicating a first-order field-driven transition between different SC states [Fig. 1(a)]. Similar phase transitions within the SC state were observed in UPt_3 [31] and CeCoIn_5 [32] and attributed to the interplay between superconductivity and competing magnetic order parameters. In CeRh_2As_2 , the presence of alternating Rashba SOC suggests the possibility of a transition from spin-singlet to spin-triplet superconductivity [33–42], although other scenarios may also apply [43, 44].

To further understand the superconducting phases of CeRh_2As_2 , we use neutron scattering to probe the low-temperature (T) zero-field magnetism of CeRh_2As_2 . Our elastic scattering data reveal no significant differences between 0.08 K and 0.8 K, indicating the absence or weakness of magnetic order, and place an upper limit of $0.31 \mu_B$ on the staggered magnetization of corresponding Néel orders at temperatures down to 0.08 K. Our inelastic magnetic neutron scattering data, however, reveal a gapless spectrum of quasi-2D AFM spin fluctuations at the (π, π) wave vector \mathbf{Q}_{AFM} extending up to 1.2 meV. In combination with density functional theory (DFT) calculations [28, 35, 37, 45–49] and angle-resolved photoemission spectroscopy (ARPES) measurements [46–48] that reveal Fermi-surface nesting at \mathbf{Q}_{AFM} , our findings suggest proximity to Fermi-surface-driven magnetic criticality in CeRh_2As_2 [22, 28], with the associated spin fluctuations playing a crucial role in the superconductivity.

* tchen115@jhu.edu

† rans@wustl.edu

‡ yusong_phys@zju.edu.cn

§ broholm@jhu.edu

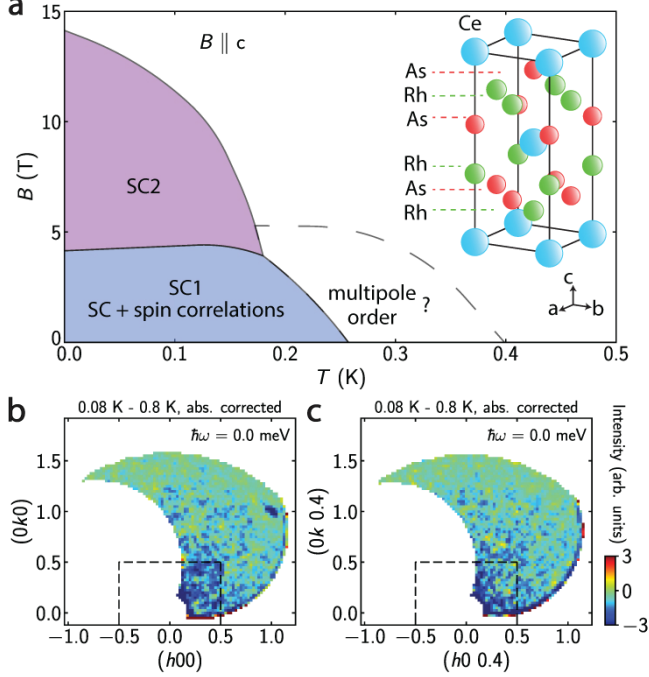


FIG. 1. (a) Schematic field-temperature phase diagram of CeRh_2As_2 for $\mathbf{B} \parallel \mathbf{c}$ based on Refs. [22, 25–30]. The inset shows the crystal structure of CeRh_2As_2 . \mathbf{Q} -dependence of the difference in elastic neutron scattering between $T = 0.08$ K and $T = 0.8$ K for (b) $|l| < 0.15$ and (c) $0.35 < |l| < 0.45$. Dashed lines indicate the Brillouin zone.

CeRh_2As_2 single crystals were synthesized via a flux method [22, 50]. The sharp resistive transition of a representative sample at $T_c = 0.3$ K is displayed in the Supplemental Material [51]. For neutron scattering experiments in the $(hk0)$ plane, ~ 120 crystals (0.9 g) were coaligned with a full width at half maximum (FWHM) mosaic width of 2.8 degrees for rotation around the \mathbf{c} axis. As detailed in Supplemental Material [51], precautions were taken to ensure good thermal contact between the dilution refrigerator and the sample. Neutron experiments were conducted at Oak Ridge National Laboratory using the CNCS Spectrometer [52] with a fixed incident energy E_i of 3.32 meV. Operating in the high flux mode with the disk chopper rotating at 180 Hz, this setup resulted in an FWHM elastic energy resolution of 0.17 meV.

Normalization of the measured scattering cross sections was achieved by comparing the count rate with the \mathbf{Q} -integrated count rate for the (110) nuclear Bragg peak. As detailed in the Supplemental Material [51], a scattering angle and energy transfer dependent factor was applied to background subtracted data to correct for the significant absorption cross section of CeRh_2As_2 . When background subtraction is not feasible, uncorrected intensity data are presented in arbitrary units. In the following, momentum transfer \mathbf{Q} is expressed as

TABLE I. Upper limits on the magnitudes of staggered magnetization in CeRh_2As_2 obtained from the difference between elastic neutron scattering at $T = 0.08$ K and $T = 0.8$ K shown in Fig. 1(b)-1(c). In-plane oriented magnetic order is harder to detect due to the domain averaged polarization factor

\mathbf{Q}_m	$m_{z,\text{max}} (\mu\text{B})$	$m_{\parallel,\text{max}} (\mu\text{B})$
$(\frac{1}{2} \frac{1}{2} 0)$	0.10	0.14
$(\frac{1}{2} \frac{1}{2} \frac{1}{2})$	0.14	0.20
(010)	0.14	0.20
$(01 \frac{1}{2})$	0.22	0.31
quasi-2D $(\frac{1}{2} \frac{1}{2})$	0.14	0.20

$\mathbf{Q} = h\mathbf{a}^* + k\mathbf{b}^* + l\mathbf{c}^*$, where (hkl) denotes Miller indices. A pair of indices (hk) specify the in-plane component of wave vector \mathbf{Q}_{\parallel} . Here, $a^* = b^* = 2\pi/a$ and $c^* = 2\pi/c$, with $a = b = 4.28$ Å and $c = 9.86$ Å at room temperature [22].

The difference in elastic scattering between data acquired in the SC state at 0.08 K and in the normal state at 0.8 K is shown in Figs. 1(b) and 1(c) for $l = 0$ and $l = \pm 0.4$, respectively. No diffraction peaks are apparent in either figure. These data place upper limits on magnetic ordering at specific magnetic wave vectors (see Table I and the Supplemental Material [51]).

Nuclear quadrupole resonance (NQR) [53] and nuclear magnetic resonance (NMR) [54] experiments provide evidence for an increase of the NQR and NMR linewidths in the low-field SC1 state for the As sites of As-Rh-As blocks, which has distinct Ce neighbors displaced along \mathbf{c} , but not for the As sites of Rh-As-Rh blocks, where Ce neighbors come in groups of four whose fields cancel out in the AFM states shown in Table I. A possible explanation is weak long- or short-range AFM ordering that is detectable with local probes such as NMR and NQR [54, 55], but sufficiently weak and/or broad in \mathbf{Q} to evade detection through neutron diffraction (see Table I).

Though we do not detect elastic magnetic diffraction, dynamic AFM spin correlations are apparent in the inelastic scattering. Figures 2(a)-(d) show the \mathbf{Q} -dependence within the (hk) plane of the scattering intensity for various fixed $\hbar\omega$. As AFM fluctuations are observed in both paramagnetic and SC states with no discernible differences within the $\hbar\omega$ -range covered, measurements taken at 0.08 K and 0.8 K are averaged and denoted as 0.4(4) K to improve statistical accuracy. The elastic data display the (110) nuclear Bragg peak from CeRh_2As_2 , which we use for normalization and alignment. Other T -independent features in the elastic scattering are associated with the sample holder (powder ring and low $|\mathbf{Q}|$ diffuse scattering) and two small misaligned CeRh_2As_2 crystallites. At $\hbar\omega = 0.35$ meV, a diffuse peak is observed near the AFM wave vector $\mathbf{Q}_{\text{AFM}} = (\frac{1}{2} \frac{1}{2})$ [Fig. 2(b)]. While the peak position persists, the intensity decreases with increasing $\hbar\omega$.

Figures 2(e) and 2(f) show constant- $\hbar\omega$ cuts through

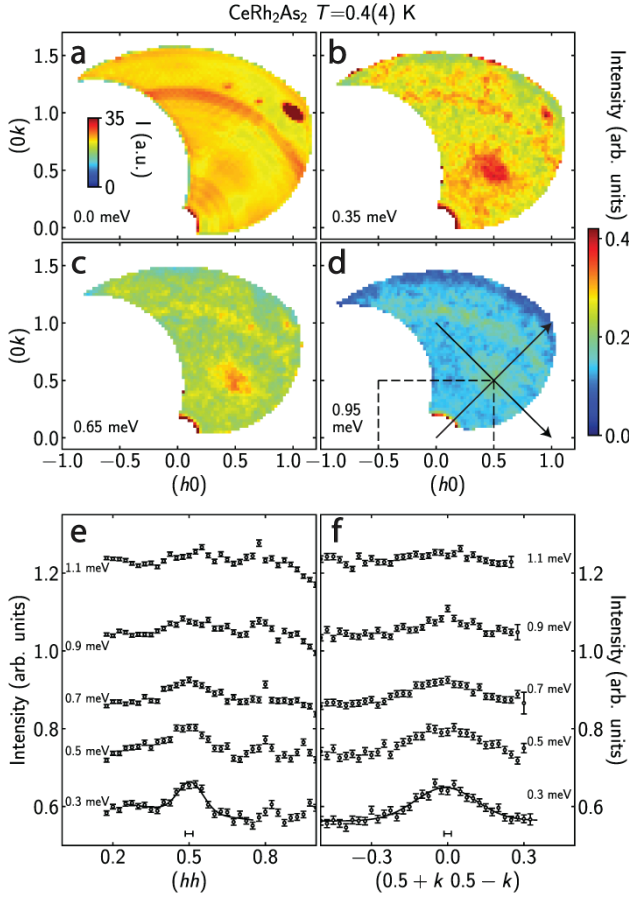


FIG. 2. (a)-(d) Q_{\parallel} -dependence of neutron scattering from CeRh_2As_2 at selected $\hbar\omega$ for $T = 0.4(4)$ K and $|Q_z| < 0.5c^*$. The energy windows are 0.4 meV in (a) and 0.3 meV in (b)-(d). Arrows indicate the longitudinal (hh) and transverse (kk) directions. (e),(f) Constant energy cuts along (hh) and (kk) through $\mathbf{Q}_{\text{AFM}} = (\frac{1}{2}, \frac{1}{2})$ for selected $\hbar\omega$ with an energy window of 0.2 meV. The averaging windows are $\Delta^2\mathbf{Q} = \pm(0.15, -0.15, 0) \pm (0, 0, 0.5)$ in (e) and $\Delta^2\mathbf{Q} = \pm(0.1, 0.1, 0) \pm (0, 0, 0.5)$ in (f). Solid lines for $\hbar\omega = 0.3$ meV are Gaussian fits. The horizontal bars represent the FWHM resolution.

these data along the longitudinal (hh) and transverse (kk) directions. These cuts show that the low-energy magnetic scattering is centered at \mathbf{Q}_{AFM} consistent with dynamic short-ranged AFM spin correlations as in many Ce-based heavy fermion systems including SC CeCoIn_5 [13]. Fitting the cuts to Gaussians, we infer dynamic correlation lengths (defined as $2/\text{FWHM}$) at 0.3 meV along (hh) and (kk) of $\xi_{hh} = 8.1(8)$ Å and $\xi_{kk} = 3.4(3)$ Å, respectively. Considering the fourfold rotation axis of paramagnetic CeRh_2As_2 , this anisotropy suggests a preferred polarization factor in the magnetic neutron scattering cross section. Specifically, scattering at \mathbf{Q}_{AFM} detects spin fluctuations in the plane perpendicular to \mathbf{Q}_{AFM} , thus along \mathbf{c} or $(1\bar{1}0)$, of which the latter component can give rise to the observed anisotropy. The data indicate an underlying nematic character to the AFM

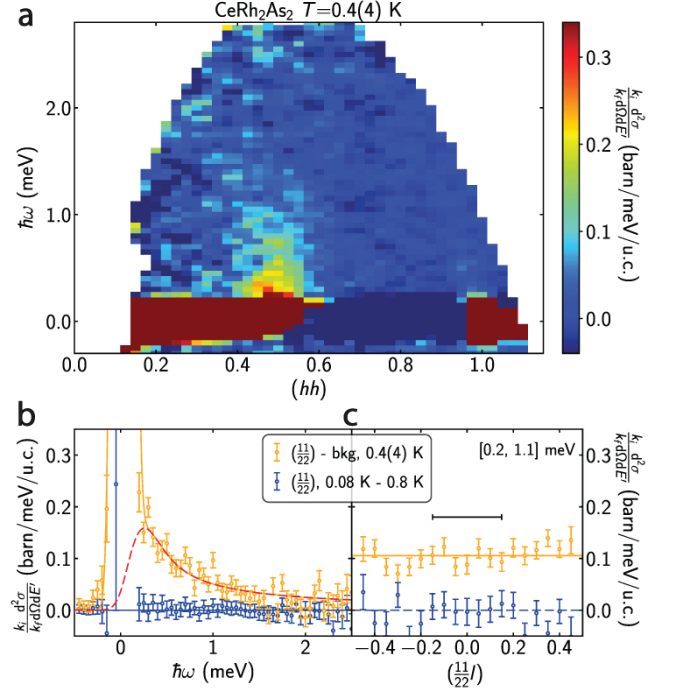


FIG. 3. (a) Background subtracted inelastic neutron scattering versus $\mathbf{Q} = (hh)$ and $\hbar\omega$ for CeRh_2As_2 at $T = 0.4(4)$ K. The signal averaging window is $\Delta^2\mathbf{Q} = (\pm 0.15, -0.15, \pm 0.5)$. The $|\mathbf{Q}|$ and $\hbar\omega$ dependent background was determined by averaging all data outside the signal volume. (b,c) Background subtracted data at $T = 0.4(4)$ K in orange and the difference between $T = 0.08$ K and $T = 0.8$ K data in blue. (b) shows an $\hbar\omega$ scan at $\mathbf{Q}_{\text{AFM}} = (\frac{1}{2}, \frac{1}{2})$ averaging over $\Delta^3\mathbf{Q} = (\pm 0.1, \pm 0.1, \pm 0.5)$. The red line shows a fit to the data described in the text. (c) shows a scan along $\mathbf{Q} = (\frac{1}{2}, \frac{1}{2})$ averaging over $\hbar\omega \in [0.2, 1.1]$ meV and $\Delta^2\mathbf{Q} = \pm(0.1, 0.1) \pm (0.15, -0.15)$. The horizontal bar represents the resolution width.

spin correlations, where the correlation length is longer perpendicular to than parallel to the fluctuating in-plane staggered magnetization. Such anisotropy can arise from symmetric anisotropic exchange interactions and was previously observed in iron-based superconductors[9]. Given the spin-orbital character of Ce-based magnetism, anisotropic interactions are indeed anticipated. The data specifically indicate in-plane anisotropic interactions and suggest that the fourfold rotation symmetry will be broken by the corresponding static order.

Figure 3(a) displays the $\mathbf{Q} - \omega$ dependent magnetic scattering cross section for $\mathbf{Q} \parallel (11)$. A ridge of low-energy excitations at \mathbf{Q}_{AFM} extending to 1.2 meV is apparent. Figure 3(b) shows a broad constant- \mathbf{Q}_{AFM} cut through these data. While data for $|\hbar\omega| < 0.15$ meV are dominated by imperfect subtraction of the incoherent elastic scattering, we associate the tail of scattering for $\hbar\omega > 0.15$ meV that is absent on the neutron energy gain side ($\hbar\omega < -0.15$ meV) with magnetic quantum fluctuations for $k_B T \ll \hbar\omega$. To further characterize the scat-

tering, we fit these data against a resolution-convoluted Lorentzian response function of the form :

$$\mathcal{S}(\omega) = \frac{1}{1 - e^{-\beta\hbar\omega}} \frac{\chi_0\Gamma\omega}{\Gamma^2 + \omega^2}, \quad (1)$$

plus a central Gaussian peak to account for the residual elastic background. As shown in Fig. 3(b), this model provides an excellent account of the data with a characteristic relaxation rate of $\hbar\Gamma = 0.10(4)$ meV. This suggests proximity to a quantum critical point (QCP) where $\hbar\Gamma \sim k_B T$ [13, 14, 56, 57].

From the total magnetic scattering associated with inelastic magnetic scattering below 2.5 meV, we obtain the dynamic moment of $1.6(4)\mu_B^2$. The reduction in moment compared to the effective moment inferred from susceptibility ($\mu_{\text{eff}}^2 = 6.55\mu_B^2$ [22]) is observed in other Ce-based heavy-fermion superconductors, such as CeCoIn₅ [13] and CeCu₂Si₂ [14]. Magnetic excitations extend to much higher energies in these systems [19, 20] due to crystal electric field and Kondo screening. Likewise, in CeRh₂As₂ we expect such interactions to define a low-energy reduced moment regime with residual AFM intersite interactions.

To probe the associated spin correlations along c , Fig. 3(c) shows the l dependence of scattering for $\hbar\omega \in [0.2, 1.1]$ meV at \mathbf{Q}_{AFM} . The corresponding count rate at $\mathbf{Q}_{\text{bkg}} = (0.1, 0.7)$ where $|\mathbf{Q}_{\text{bkg}}| = |\mathbf{Q}_{\text{AFM}}|$ was used as background. The inelastic scattering at \mathbf{Q}_{AFM} consistently exceeds that at \mathbf{Q}_{bkg} by a nearly l -independent amount, indicating quasi-2D spin correlations. No difference between scattering at 0.08 K and 0.8 K is observed in the accessible energy range.

To gain insights into the origin of the AFM spin fluctuations in CeRh₂As₂, we conducted band structure calculations using DFT, treating Ce 4*f* electrons as core states. The results are shown in Fig. 4(a), with the corresponding Fermi surface displayed in Figs. 4(b)-4(d). Specifically, the Fermi surface at $l = 0$ [Fig. 4(c)] is squarelike, with sides approximately connected by \mathbf{Q}_{AFM} , as indicated by the red arrow. Since Ce 4*f* electrons are treated as core states, the calculated Fermi surface arises from conduction electrons that induce a Ruderman-Kittel-Kasuya-Yosida interaction between Ce 4*f* local moments, leading to AFM spin fluctuations at \mathbf{Q}_{AFM} . Although the strong k_z dependence of the DFT Fermi surface seems at odds with the quasi-2D character of the AFM fluctuations observed in our experiments, this discrepancy suggests the dominance of in-plane correlations, which is crucial in theoretical models predicting the singlet-triplet transition in CeRh₂As₂ [33–42]. Alternatively, as CeRh₂As₂ is a heavy fermion metal with 4*f* states that hybridize with the conduction bands, the spin fluctuations at \mathbf{Q}_{AFM} may arise from particle-hole excitations of the heavy electron bands. The quasi-2D AFM fluctuations observed in our neutron scattering measurements uniquely identifies (π, π) as the primary nesting vector, among other plausible nesting vectors suggested by recent ARPES studies [46–48].

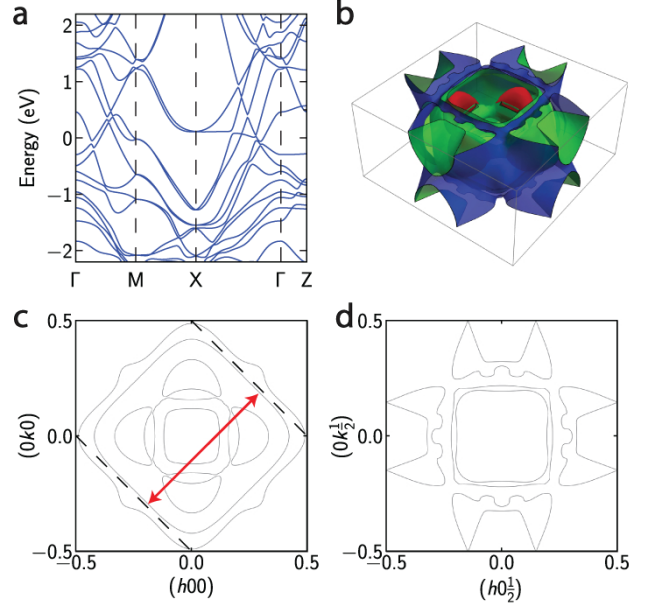


FIG. 4. (a) Electronic band structure of CeRh₂As₂ calculated using DFT with Ce 4*f* electrons in the core. (b)-(d) The corresponding Fermi surface as a 3D image and as 2D slices through (c) the $(hk0)$ plane and (d) the $(hk\frac{1}{2})$ plane. The red arrow indicates the wave vector $\mathbf{Q}_{\text{AFM}} = (\frac{1}{2}, \frac{1}{2})$ associated with low energy inelastic magnetic neutron scattering [Fig. 3(a)], which is seen to connect significant portions of the DFT Fermi surface.

Resistivity and specific heat measurements reveal non-Fermi-liquid behavior at low T , which indicates proximity to a QCP [22, 28]. Our observations of anisotropic AFM fluctuations in CeRh₂As₂ suggest that this QCP has a nematic 2D AFM character, where the proximate ordered phase likely breaks the fourfold rotational symmetry of the underlying crystal lattice. Quantum critical fluctuations near a QCP are natural candidates as bosonic modes that drive superconductivity. Accordingly, our findings highlight the prominent role of AFM spin fluctuations in the superconductivity of CeRh₂As₂, as in many other heavy-fermion superconductors. The momentum and energy dependence of the spin fluctuations in CeRh₂As₂ revealed in our work provide stringent constraints on models of its zero-field superconductivity.

Time reversal and inversion symmetry in a metal enable even parity spin-singlet superconductivity and odd parity spin-triplet superconductivity, respectively. However, in superconductors lacking global inversion symmetry, electronic antisymmetric SOC, such as Rashba SOC, lift the spin degeneracy and mix spin-singlet and spin-triplet states [58, 59]. The unique local inversion symmetry breaking of CeRh₂As₂ naturally connects it to the previous proposal of noncentrosymmetric superconductivity in CeCoIn₅ multilayers [32]. Alternating Rashba SOC has been known to support distinct SC phases with spin-singlet and spin-triplet symmetries in the field-

temperature phase diagram [24, 58]. Experimental results in CeRh_2As_2 appear consistent with this picture, suggesting that the SC1 and high-field SC2 phases correspond to spin-singlet and spin-triplet pairing states, respectively. However, the recent NMR study [54] reported T -dependent Knight shifts, suggesting spin-singlet pairing in both SC phases, adding complexity to the Rashba SOC scenario. Since AFM spin fluctuations are typically seen in spin-singlet unconventional superconductors and ferromagnetic spin fluctuations are expected for spin-triplet superconductors, our observation of AFM spin fluctuations at zero field is consistent with spin-singlet pairing in the SC1 phase. The fact that these AFM fluctuations extend to $1.2 \text{ meV} \gg k_B T_C$ suggests they will persist in the field-induced SC2 phase. In such a scenario, the SC2 phase should exhibit a prominent spin-singlet pairing component, consistent with the NMR measurement [54]. However, as research on UTe_2 revealed, AFM spin fluctuations can mediate spin-triplet superconductivity [15]. Thus, additional theoretical and experimental efforts are necessary to elucidate the symmetry and mechanism of the SC2 phase. Nevertheless, our observation of AFM spin fluctuations places strong constraints on models of its field-induced superconductor-superconductor transition.

We have investigated the magnetic excitations in CeRh_2As_2 using neutron scattering, revealing nematic quasi-2D AFM spin fluctuations centered at \mathbf{Q}_{AFM} and extending up to 1.2 meV at low T . Our neutron scattering measurements and DFT calculations indicate \mathbf{Q}_{AFM}

fluctuations result from the nesting of heavy quasi-2D Ce $4f$ electrons, which are also responsible for the heavy-fermion superconductivity in CeRh_2As_2 . These findings indicate a crucial role of AFM spin fluctuations in the superconductivity of CeRh_2As_2 , although the connection to the field-induced superconductor-superconductor transition remains to be understood.

Acknowledgments - We gratefully acknowledge the support from T. Xie, and R. Kumar during the experiments and the valuable discussions with S.-H. Baek, P. Dai, Y. Liu, E. Hassinger, and D. Agterberg. Work at the Institute for Quantum Matter, was supported by DOE, Office of Science, Basic Energy Sciences under Award No. DE-SC0019331 and DE-SC0024469. Research at Washington University was supported by the National Science Foundation (NSF) Division of Materials Research Award DMR-2236528. Research at the University of Maryland was supported by the U.S. Department of Energy (DOE) Award No. DE-SC-0019154 (experimental preparation). J.P. acknowledges support from the Gordon and Betty Moore Foundation's EPIQS Initiative through Grant No. GBMF4419. C.B. was supported by the Gordon and Betty Moore Foundation EPIQS program under GBMF9456 and acknowledges the hospitality of the Instituto de Física at UNAM, México. Research at Zhejiang University was supported by the National Key R&D Program of China (No. 2022YFA1402200). A portion of this research used resources at the Spallation Neutron Source, a DOE Office of Science User Facility operated by ORNL.

-
- [1] T. Moriya and K. Ueda, Spin fluctuations and high temperature superconductivity, *Advances in Physics* **49**, 555 (2000).
 - [2] D. J. Scalapino, A common thread: The pairing interaction for unconventional superconductors, *Reviews of Modern Physics* **84**, 1383 (2012).
 - [3] J. Rossat-Mignod, L. Regnault, C. Vettier, P. Bourges, P. Burlet, J. Bossy, J. Henry, and G. Lapertot, Neutron scattering study of the $\text{YBa}_2\text{Cu}_3\text{O}_{6+x}$ system, *Physica C: Superconductivity* **185**, 86 (1991).
 - [4] H. Mook, M. Yethiraj, G. Aeppli, T. Mason, and T. Armstrong, Polarized neutron determination of the magnetic excitations in $\text{YBa}_2\text{Cu}_3\text{O}_7$, *Physical Review Letters* **70**, 3490 (1993).
 - [5] H. F. Fong, B. Keimer, P. W. Anderson, D. Reznik, F. Doğan, and I. A. Aksay, Phonon and magnetic neutron scattering at 41 meV in $\text{YBa}_2\text{Cu}_3\text{O}_7$, *Physical Review Letters* **75**, 316 (1995).
 - [6] J. M. Tranquada, G. Xu, and I. A. Zaliznyak, Superconductivity, antiferromagnetism, and neutron scattering, *Journal of Magnetism and Magnetic Materials* **350**, 148 (2014).
 - [7] A. Christianson, E. Goremychkin, R. Osborn, S. Rosenkranz, M. Lumsden, C. Malliakas, I. Todorov, H. Claus, D. Chung, M. Kanatzidis, *et al.*, Unconventional superconductivity in $\text{Ba}_{0.6}\text{K}_{0.4}\text{Fe}_2\text{As}_2$ from inelastic neutron scattering, *Nature* **456**, 930 (2008).
 - [8] D. Inosov, J. Park, P. Bourges, D. Sun, Y. Sidis, A. Schneidewind, K. Hradil, D. Haug, C. Lin, B. Keimer, *et al.*, Normal-state spin dynamics and temperature-dependent spin-resonance energy in optimally doped $\text{BaFe}_{1.85}\text{Co}_{0.15}\text{As}_2$, *Nature Physics* **6**, 178 (2010).
 - [9] P. Dai, Antiferromagnetic order and spin dynamics in iron-based superconductors, *Reviews of Modern Physics* **87**, 855 (2015).
 - [10] Q. Wang, Y. Shen, B. Pan, Y. Hao, M. Ma, F. Zhou, P. Steffens, K. Schmalzl, T. Forrest, M. Abdel-Hafiez, *et al.*, Strong interplay between stripe spin fluctuations, nematicity and superconductivity in FeSe , *Nature Materials* **15**, 159 (2016).
 - [11] T. Chen, Y. Chen, A. Kreisel, X. Lu, A. Schneidewind, Y. Qiu, J. Park, T. G. Perring, J. R. Stewart, H. Cao, *et al.*, Anisotropic spin fluctuations in detwinned FeSe , *Nature Materials* **18**, 709 (2019).
 - [12] M. Smidman, O. Stockert, E. M. Nica, Y. Liu, H. Yuan, Q. Si, and F. Steglich, Colloquium: Unconventional fully gapped superconductivity in the heavy-Fermion metal CeCu_2Si_2 , *Reviews of Modern Physics* **95**, 031002 (2023).
 - [13] C. Stock, C. Broholm, J. Hudis, H. J. Kang, and C. Petrovic, Spin resonance in the d-wave superconductor CeCoIn_5 , *Physical Review Letters* **100**, 087001 (2008).
 - [14] O. Stockert, J. Arndt, E. Faulhaber, C. Geibel, H. S. Jeevan, S. Kirchner, M. Loewenhaupt, K. Schmalzl, W. Schmidt, Q. Si, *et al.*, Magnetically driven supercon-

- ductivity in CeCu_2Si_2 , *Nature Physics* **7**, 119 (2011).
- [15] C. Duan, R. Baumbach, A. Podlesnyak, Y. Deng, C. Moir, A. J. Breindel, M. B. Maple, E. Nica, Q. Si, and P. Dai, Resonance from antiferromagnetic spin fluctuations for superconductivity in UTe_2 , *Nature* **600**, 636 (2021).
 - [16] L. Regnault, W. Erkelens, J. Rossat-Mignod, P. Lejay, and J. Flouquet, Neutron scattering study of the heavy-Fermion compound CeRu_2Si_2 , *Physical Review B* **38**, 4481 (1988).
 - [17] J. Arndt, O. Stockert, K. Schmalzl, E. Faulhaber, H. S. Jeevan, C. Geibel, W. Schmidt, M. Loewenhaupt, and F. Steglich, Spin fluctuations in normal state CeCu_2Si_2 on approaching the quantum critical point, *Physical Review Letters* **106**, 246401 (2011).
 - [18] Q. Wang, Y. Shen, B. Pan, X. Zhang, K. Ikeuchi, K. Iida, A. Christianson, H. Walker, D. Adroja, M. Abdel-Hafiez, *et al.*, Magnetic ground state of FeSe , *Nature Communications* **7**, 12182 (2016).
 - [19] Y. Song, W. Wang, J. S. Van Dyke, N. Pouse, S. Ran, D. Yazici, A. Schneidewind, P. Čermák, Y. Qiu, M. Maple, *et al.*, Nature of the spin resonance mode in CeCoIn_5 , *Communications Physics* **3**, 98 (2020).
 - [20] Y. Song, W. Wang, C. Cao, Z. Yamani, Y. Xu, Y. Sheng, W. Löser, Y. Qiu, Y.-f. Yang, R. J. Birgeneau, *et al.*, High-energy magnetic excitations from heavy quasiparticles in CeRu_2Si_2 , *npj Quantum Materials* **6**, 60 (2021).
 - [21] S. Carr, *Diverse Neutron Scattering Measurements in Unconventional Superconductors* (2016).
 - [22] S. Khim, J. Landaeta, J. Banda, N. Bannor, M. Brando, P. Brydon, D. Hafner, R. Kuchler, R. Cardoso-Gil, U. Stockert, *et al.*, Field-induced transition within the superconducting state of CeRh_2As_2 , *Science* **373**, 1012 (2021).
 - [23] G. Bihlmayer, P. Noël, D. V. Vyalikh, E. V. Chulkov, and A. Manchon, Rashba-like physics in condensed matter, *Nature Reviews Physics* **4**, 642 (2022).
 - [24] M. H. Fischer, M. Sigrist, D. F. Agterberg, and Y. Yanase, Superconductivity and local inversion-symmetry breaking, *Annual Review of Condensed Matter Physics* **14**, 153 (2023).
 - [25] J. Landaeta, P. Khanenko, D. Cavanagh, C. Geibel, S. Khim, S. Mishra, I. Sheikin, P. Brydon, D. Agterberg, M. Brando, *et al.*, Field-angle dependence reveals odd-parity superconductivity in CeRh_2As_2 , *Physical Review X* **12**, 031001 (2022).
 - [26] S. Mishra, Y. Liu, E. D. Bauer, F. Ronning, and S. M. Thomas, Anisotropic magnetotransport properties of the heavy-Fermion superconductor CeRh_2As_2 , *Physical Review B* **106**, L140502 (2022).
 - [27] S. Onishi, U. Stockert, S. Khim, J. Banda, M. Brando, and E. Hassinger, Low-temperature thermal conductivity of the two-phase superconductor CeRh_2As_2 , *Frontiers in Electronic Materials* **2**, 880579 (2022).
 - [28] D. Hafner, P. Khanenko, E.-O. Eljaouhari, R. Kuchler, J. Banda, N. Bannor, T. Lühmann, J. Landaeta, S. Mishra, I. Sheikin, *et al.*, Possible quadrupole density wave in the superconducting Kondo lattice CeRh_2As_2 , *Physical Review X* **12**, 011023 (2022).
 - [29] K. Semeniuk, D. Hafner, P. Khanenko, T. Lühmann, J. Banda, J. Landaeta, C. Geibel, S. Khim, E. Hassinger, and M. Brando, Decoupling multiphase superconductivity from normal state ordering in CeRh_2As_2 , *Physical Review B* **107**, L220504 (2023).
 - [30] G. Chajewski and D. Kaczorowski, Discovery of magnetic phase transitions in heavy-Fermion superconductor CeRh_2As_2 , *Physical Review Letters* **132**, 076504 (2024).
 - [31] G. Aeppli, D. Bishop, C. Broholm, E. Bucher, K. Siemensmeyer, M. Steiner, and N. Stüsser, Magnetic order in the different superconducting states of Upt 3, *Physical Review Letters* **63**, 676 (1989).
 - [32] T. Yoshida, M. Sigrist, and Y. Yanase, Pair-density wave states through spin-orbit coupling in multilayer superconductors, *Physical Review B* **86**, 134514 (2012).
 - [33] E. G. Schertenleib, M. H. Fischer, and M. Sigrist, Unusual h- t phase diagram of CeRh_2As_2 : The role of staggered noncentrosymmetry, *Physical Review Research* **3**, 023179 (2021).
 - [34] A. Skurativska, M. Sigrist, and M. H. Fischer, Spin response and topology of a staggered-rashba superconductor, *Physical Review Research* **3**, 033133 (2021).
 - [35] K. Nogaki, A. Daido, J. Ishizuka, and Y. Yanase, Topological crystalline superconductivity in locally noncentrosymmetric CeRh_2As_2 , *Physical Review Research* **3**, L032071 (2021).
 - [36] D. Möckli and A. Ramires, Superconductivity in disordered locally noncentrosymmetric materials: An application to CeRh_2As_2 , *Physical Review B* **104**, 134517 (2021).
 - [37] D. Cavanagh, T. Shishidou, M. Weinert, P. Brydon, and D. F. Agterberg, Nonsymmorphic symmetry and field-driven odd-parity pairing in CeRh_2As_2 , *Physical Review B* **105**, L020505 (2022).
 - [38] K. Nogaki and Y. Yanase, Even-odd parity transition in strongly correlated locally noncentrosymmetric superconductors: Application to CeRh_2As_2 , *Physical Review B* **106**, L100504 (2022).
 - [39] D. Cavanagh, D. F. Agterberg, and P. Brydon, Pair breaking in superconductors with strong spin-orbit coupling, *Physical Review B* **107**, L060504 (2023).
 - [40] Y. Yanase, A. Daido, K. Takasan, and T. Yoshida, Topological d-wave superconductivity in two dimensions, *Physica E: Low-dimensional Systems and Nanostructures* **140**, 115143 (2022).
 - [41] H. G. Suh, Y. Yu, T. Shishidou, M. Weinert, P. Brydon, and D. F. Agterberg, Superconductivity of anomalous pseudospin in nonsymmorphic materials, *Physical Review Research* **5**, 033204 (2023).
 - [42] A. L. Szabó, M. H. Fischer, and M. Sigrist, Effects of nucleation at a first-order transition between two superconducting phases: Application to CeRh_2As_2 , *Physical Review Research* **6**, 023080 (2024).
 - [43] K. Machida, Violation of pauli-clogston limit in the heavy-Fermion superconductor CeRh_2As_2 : Duality of itinerant and localized 4f electrons, *Physical Review B* **106**, 184509 (2022).
 - [44] T. Hazra and P. Coleman, Triplet pairing mechanisms from Hund's-Kondo models: Applications to UTe_2 and CeRh_2As_2 , *Physical Review Letters* **130**, 136002 (2023).
 - [45] A. Ptok, K. J. Kapcia, P. T. Jochym, J. Łażewski, A. M. Oleś, and P. Piekarz, Electronic and dynamical properties of CeRh_2As_2 : Role of Rh_2As_2 layers and expected orbital order, *Physical Review B* **104**, L041109 (2021).
 - [46] Y. Wu, Y. Zhang, S. Ju, Y. Hu, Y. Huang, Y. Zhang, H. Zhang, H. Zheng, G. Yang, E.-O. Eljaouhari, *et al.*, Fermi surface nesting with heavy quasiparticles in the locally noncentrosymmetric superconductor CeRh_2As_2 , *Chinese Physics Letters* **41**, 097403 (2024).

- [47] X. Chen, L. Wang, J. Ishizuka, R. Zhang, K. Nogaki, Y. Cheng, F. Yang, Z. Chen, F. Zhu, Z. Liu, *et al.*, Coexistence of near- E_F flat band and van Hove singularity in a two-phase superconductor, *Physical Review X* **14**, 021048 (2024).
- [48] B. Chen, H. Liu, Q.-Y. Wu, C. Zhang, X.-Q. Ye, Y.-Z. Zhao, J.-J. Song, X.-Y. Tian, B.-L. Tan, Z.-T. Liu, *et al.*, Exploring possible fermi surface nesting and the nature of heavy quasiparticles in the spin-triplet superconductor candidate CeRh_2As_2 , *Physical Review B* **110**, L041120 (2024).
- [49] J. Ishizuka, K. Nogaki, M. Sigrist, and Y. Yanase, Correlation-induced fermi surface evolution and topological crystalline superconductivity in CeRh_2As_2 , *Physical Review B* **110**, L140505 (2024).
- [50] H. Siddiquee, Z. Rehfuss, C. Broyles, and S. Ran, Pressure dependence of superconductivity in CeRh_2As_2 , *Physical Review B* **108**, L020504 (2023).
- [51] See Supplemental Material at <url> which includes Refs. [60–64] for sample characterization, data normalization, and nesting function calculation.
- [52] G. Ehlers, A. A. Podlesnyak, J. L. Niedziela, E. B. Iverson, and P. E. Sokol, The new cold neutron chopper spectrometer at the spallation neutron source: Design and performance, *Review of Scientific Instruments* **82** (2011).
- [53] M. Kibune, S. Kitagawa, K. Kinjo, S. Ogata, M. Manago, T. Taniguchi, K. Ishida, M. Brando, E. Hassinger, H. Rosner, *et al.*, Observation of antiferromagnetic order as odd-parity multipoles inside the superconducting phase in CeRh_2As_2 , *Physical Review Letters* **128**, 057002 (2022).
- [54] S. Ogata, S. Kitagawa, K. Kinjo, K. Ishida, M. Brando, E. Hassinger, C. Geibel, and S. Khim, Parity transition of spin-singlet superconductivity using sublattice degrees of freedom, *Physical Review Letters* **130**, 166001 (2023).
- [55] S. Kitagawa, M. Kibune, K. Kinjo, M. Manago, T. Taniguchi, K. Ishida, M. Brando, E. Hassinger, C. Geibel, and S. Khim, Two-dimensional xy-type magnetic properties of locally noncentrosymmetric superconductor CeRh_2As_2 , *Journal of the Physical Society of Japan* **91**, 043702 (2022).
- [56] C. Broholm, J. Kjems, G. Aeppli, Z. Fisk, J. Smith, S. Shapiro, G. Shirane, and H. Ott, Spin fluctuations in the antiferromagnetic heavy-Fermion system U_2Zn_{17} , *Physical Review Letters* **58**, 917 (1987).
- [57] O. Stockert, E. Faulhaber, K. Schmalzl, W. Schmidt, H. Jeevan, M. Deppe, C. Geibel, T. Cichorek, T. Nakanishi, M. Loewenhaupt, *et al.*, Peculiarities of the antiferromagnetism in CeCu_2Si_2 , in *Journal of Physics: Conference Series*, Vol. 51 (IOP Publishing, 2006) p. 211.
- [58] E. M. Nica, S. Ran, L. Jiao, and Q. Si, Multiple superconducting phases in heavy-Fermion metals, *Frontiers in Electronic Materials* **2**, 944873 (2022).
- [59] L. P. Gor'kov and E. I. Rashba, Superconducting 2D system with lifted spin degeneracy: mixed singlet-triplet state, *Physical Review Letters* **87**, 037004 (2001).
- [60] T. Hahn, U. Shmueli, and J. W. Arthur, *International tables for crystallography*, Vol. 1 (Reidel Dordrecht, 1983).
- [61] O. Arnold, J.-C. Bilheux, J. Borreguero, A. Buts, S. I. Campbell, L. Chapon, M. Doucet, N. Draper, R. F. Leal, M. Gigg, *et al.*, Mantid—data analysis and visualization package for neutron scattering and μSR experiments, *Nuclear Instruments and Methods in Physics Research Section A: Accelerators, Spectrometers, Detectors and Associated Equipment* **764**, 156 (2014).
- [62] C. Dwiggins, Rapid calculation of x-ray absorption correction factors for cylinders to an accuracy of 0.1%, *Acta Crystallographica Section A: Crystal Physics, Diffraction, Theoretical and General Crystallography* **31**, 146 (1975).
- [63] NIST center for neutron research tabulated neutron scattering lengths and cross sections, <https://www.ncnr.nist.gov/resources/n-lengths/list.html>.
- [64] V. F. Sears, Neutron scattering lengths and cross sections, *Neutron News* **3**, 26 (1992).

Supplemental Material for Antiferromagnetic Spin Fluctuations in the Spin-Triplet Superconductor Candidate CeRh_2As_2

Tong Chen,^{*} Hasan Siddiquee, Qiaozhi Xu, Zack Reh fuss, Shiyuan Gao, Chris Lygouras, Jack Drouin, Vincent Morano, Keenan E. Avers, Christopher J. Schmitt, Andrey Podlesnyak, Johnpierre Paglione, Sheng Ran,[†] Yu Song,[‡] and Collin Broholm[§]
(Dated: December 11, 2024)

I. SAMPLE ALIGNMENT, AND X-RAY LAUE PATTERN

High-quality single crystals of CeRh_2As_2 were synthesized using Bi flux methods, as described in [1]. Representative resistivity plots are shown in Figures S1(a,b). These single crystals typically manifest as octagonal plates with dimensions of $1.0 \text{ mm} \times 1.0 \text{ mm} \times 0.2 \text{ mm}$. Natural edges align along either (110) or (100) directions, while the out-of-plane direction corresponds to (001), the \mathbf{c} -axis (Fig. S1(c)). A total mass of 0.9 g, comprising approximately 120 pieces of CeRh_2As_2 single crystals, was co-aligned on two oxygen-free high conductivity (OFHC) copper plates using CYTOP for attachment. Thermally shielded by OFHC copper foil secured to the OFHC base, the sample mount was attached to the cold finger of a dilution refrigerator with 80 μW cooling power at 100 mK (Fig. S2).

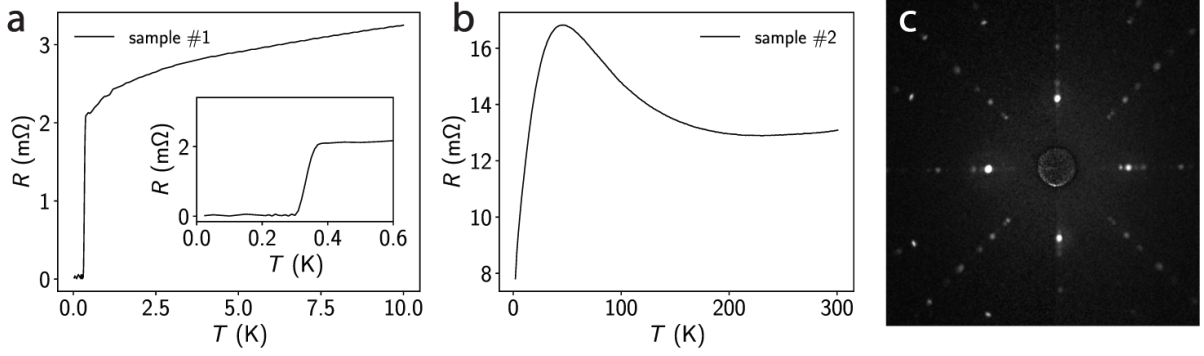


FIG. S1. (a) Temperature-dependent resistivity of CeRh_2As_2 . The inset highlights the approximate 0.3 K superconductivity offset. (b) Temperature-dependent resistivity of CeRh_2As_2 up to 300 K. (c) X-ray Laue pattern of a CeRh_2As_2 single crystal, displaying the crystallographic orientation within the ab -plane.

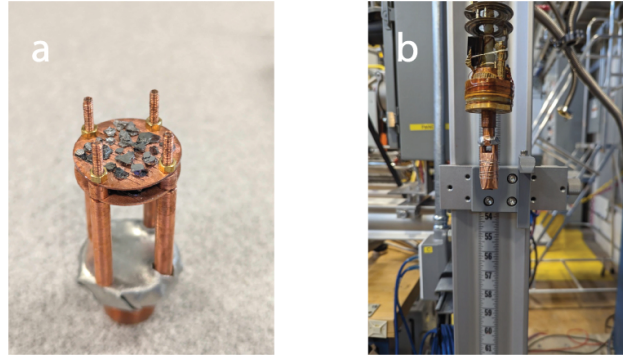


FIG. S2. (a) Photo depicting the assembly aligned in the $(hk0)$ scattering plane for CNCS. (b) Photo showing the assembly with an oxygen-free high conductivity (OFHC) copper shielding attached to the cold finger of a dilution refrigerator.

^{*} tchen115@jhu.edu

[†] rans@wustl.edu

[‡] yusong.phys@zju.edu.cn

[§] broholm@jhu.edu

II. ABSOLUTE NORMALIZATION

The monitor normalized scattering intensity obtained from initial data reduction is related to the scattering cross-section as follows:

$$\mathcal{I}(\mathbf{Q}, \omega) = NC \frac{k_i}{k_f} \overline{\frac{d^2\sigma}{d\Omega dE_f}}(\mathbf{Q}, \omega) \quad (1)$$

Here NC is a configuration-dependent normalization constant that is proportional to the number of unit cells in the sample (N). The bar indicates convolution with the instrumental resolution function:

$$\overline{\frac{d^2\sigma}{d\Omega dE_f}}(\mathbf{Q}, \omega) = \int d^3\mathbf{Q}' \hbar d\omega' \mathcal{R}_{\mathbf{Q}, \omega}(\mathbf{Q} - \mathbf{Q}', \omega - \omega') \frac{d^2\sigma}{d\Omega dE_f}(\mathbf{Q}', \omega') \quad (2)$$

$\mathcal{R}_{\mathbf{Q}, \omega}$ is sharply peaked when its arguments vanish and unity normalized:

$$\int d^3\mathbf{Q}' \hbar d\omega' \mathcal{R}_{\mathbf{Q}, \omega}(\mathbf{Q} - \mathbf{Q}', \omega') \equiv 1 \quad (3)$$

Absolute normalization of the scattering cross-section was achieved using the integrated intensity of the (110) nuclear Bragg reflection. This has the advantage of being unaffected by sample absorption for the elastic channel. The Bragg scattering cross section per unit cell of volume v_N is given by (Fig. S3(a)):

$$\left(\frac{d^2\sigma}{d\Omega dE_f} \right)_{\text{el}}^{\text{nuc}} = \frac{(2\pi)^3}{v_N} \sum_{\boldsymbol{\tau}} |\mathbb{F}_N(\boldsymbol{\tau})|^2 \delta(\mathbf{Q} - \boldsymbol{\tau}) \delta(\hbar\omega), \quad (4)$$

where $\mathbb{F}_N(\boldsymbol{\tau})$ is the structure factor given by:

$$\mathbb{F}_N(\boldsymbol{\tau}) = \sum_{\mathbf{d}} b_{\mathbf{d}} \exp(-2W_{\mathbf{d}}(\mathbf{Q})) \exp(i\boldsymbol{\tau} \cdot \mathbf{d}). \quad (5)$$

Here $b_{\mathbf{d}}$ is the bound coherent scattering length and $\exp(-2W_{\mathbf{d}}(\mathbf{Q}))$ is the Debye-Waller factor for the atom on the site \mathbf{d} within the unit cell with volume v_N . The scattering intensity near the $\boldsymbol{\tau} = (110)$ Bragg peak is thus given by

$$\mathcal{I}_N(\mathbf{Q}, \omega) = NC \frac{(2\pi)^3}{v_N} |\mathbb{F}_N(\boldsymbol{\tau})|^2 \mathcal{R}_{\boldsymbol{\tau}, 0}(\mathbf{Q} - \boldsymbol{\tau}, \omega). \quad (6)$$

Using the normalization property of the resolution function we find

$$NC = \int_{\mathbf{Q} \approx \boldsymbol{\tau}, \omega \approx 0} d^3\mathbf{Q} \hbar d\omega \mathcal{I}_N(\mathbf{Q}, \omega) \left(\frac{(2\pi)^3}{v_N} |\mathbb{F}_N(\boldsymbol{\tau})|^2 \right)^{-1} \quad (7)$$

We thus obtain the following expression relating the measured neutron scattering intensity to the resolution smeared absolute normalized scattering cross-section per unit cell:

$$\frac{k_i}{k_f} \overline{\frac{d^2\sigma}{d\Omega dE_f}}(\mathbf{Q}, \omega) = \frac{\mathcal{I}(\mathbf{Q}, \omega)}{\int_{\boldsymbol{\tau}} d^3\mathbf{Q} \hbar d\omega \mathcal{I}_N(\mathbf{Q}, \omega)} \frac{(2\pi)^3}{v_N} |\mathbb{F}_N(\boldsymbol{\tau})|^2 \quad (8)$$

If we denote by $\overline{\mathcal{I}_N(110)}$ the average (110) nuclear Bragg intensity throughout a volume of $\mathbf{Q} - \omega$ space that exceeds the resolution volume and has dimensions $\Delta h, \Delta k, \Delta l$ in reciprocal lattice units and $\Delta \hbar\omega$ in energy, this expression simplifies to

$$\frac{k_i}{k_f} \overline{\frac{d^2\sigma}{d\Omega dE_f}}(\mathbf{Q}, \omega) = \frac{\mathcal{I}(\mathbf{Q}, \omega)}{\overline{\mathcal{I}_N(110)} \Delta h \Delta k \Delta l \Delta \hbar\omega} |\mathbb{F}_N(\boldsymbol{\tau})|^2 \quad (9)$$

for orthogonal reciprocal lattice vectors.

III. ABSORPTION CORRECTION

When a neutron beam travels through the sample, the decrease in scattering intensity due to the absorption cross-section is quantified by the transmission coefficient:

$$A = \frac{1}{V} \int \exp(-\mu T) dV, \quad (10)$$

where μ is the attenuation length, and the integration is over the volume of the crystal. Here, T denotes the path length of the neutron beam within the crystal, encompassing the cumulative path lengths of both the incident and outgoing neutrons [2, 3].

For the scattered neutron intensity within the equatorial plane of a cylinder with radius R in the neutron beam, the expression for the transmission coefficient is:

$$A(\sigma_r, \rho, \lambda_i, \lambda_f, R, \theta) = \frac{1}{\pi R^2} \int_0^R \int_0^{2\pi} \exp(-\mu(\lambda_i)\{[R^2 - r^2 \sin^2(\phi + \theta)]^{1/2} + r \cos(\phi + \theta)\} - \mu(\lambda_f)\{[R^2 - r^2 \sin^2(\phi - \theta)]^{1/2} - r \cos(\phi - \theta)\}) r dr d\phi, \quad (11)$$

$$\mu(\lambda) = \rho * \sigma(\lambda) = \rho * \sigma_r \frac{\lambda}{1.7982 \text{ \AA}},$$

where ρ is the atomic number density of the sample and σ_r is the absorption cross-section for the reference wavelength of 1.7982 Å. Thus, the transmission coefficient A is a function of σ_r , ρ , the wavelengths of the incident and outgoing neutrons λ_i and λ_f , the radius of the cylinder sample R , and the scattering angle θ . The calculated transmission coefficients agree with those obtained through numerical integration [4]. For CeRh₂As₂,

$$\rho = \frac{M}{V} \frac{N_A}{m} = 9.05 \text{ g/cm}^3 * \frac{6.023 \times 10^{23} \text{ mol}^{-1}}{492.109 \text{ g/mol}} = 0.01108 \text{ \AA}^{-3}, \quad (12)$$

where $\frac{M}{V}$ is the density, N_A is Avogadro's constant, and m is the molecular weight. From the data on the NIST website [5, 6], we have $\sigma_r = 299.23$ barn/f.u. and in our experimental setup, the sample assembly resembles a cylinder with $R = 3.5$ mm. With $\sigma_r = 299.23$ barn/f.u., $\rho = 0.01108 \text{ \AA}^{-3}$, $\lambda_i = 4.964$ Å, and $R = 3.5$ mm, the transmission coefficient A (Eq. 11) depends on θ and λ_f , which is thus a function of \mathbf{Q} and ω .

Since we performed the absolute normalization using the (110) nuclear Bragg peak, the absorption correction is conducted by comparing the absorption coefficient $A(\mathbf{Q}, \omega)$ with that of the (110) peak. After the absorption correction, Equation 9 becomes:

$$\frac{k_i}{k_f} \frac{d^2 \sigma}{d\Omega dE_f}(\mathbf{Q}, \omega) = \frac{\mathcal{I}(\mathbf{Q}, \omega)}{\mathcal{I}_N(110) \Delta h \Delta k \Delta l \Delta \hbar \omega} \frac{A(\boldsymbol{\tau}, 0)}{A(\mathbf{Q}, \omega)} |\mathbb{F}_N(\boldsymbol{\tau})|^2, \quad (13)$$

where $A(\boldsymbol{\tau}, 0) = A(\boldsymbol{\tau} = (110), \omega = 0) = 0.0671$.

IV. UPPER BOUND OF ORDERED MOMENT

While our experiment did not detect elastic magnetic Bragg diffraction in CeRh₂As₂, the small sample neutron absorbing sample means that this does not set a particularly strict limit on the staggered magnetization of possible magnetic ordering in the sample. To determine the limits on any ordered moment set by our experiment we start by the following general expression for the elastic magnetic scattering cross section.

$$\left(\frac{d^2 \sigma}{d\Omega dE_f} \right)_{\text{el}}^{\text{mag}} = \left(\frac{\gamma r_0}{2} \right)^2 |gF(\mathbf{Q})|^2 \sum_{\alpha\beta} (\delta_{\alpha\beta} - \hat{Q}_\alpha \hat{Q}_\beta) \frac{1}{N} \sum_{RdR'd'} \langle S_{Rd}^\alpha \rangle \langle S_{R'd'}^\beta \rangle e^{i\mathbf{Q} \cdot (\mathbf{R} + \mathbf{d} - \mathbf{R}' - \mathbf{d}')} \delta(\hbar\omega) \quad (14)$$

$$= \left(\frac{\gamma r_0}{2} \right)^2 |gF(\mathbf{Q})|^2 (1 - \hat{Q}_z^2) \frac{1}{N} \sum_{RdR'd'} \langle S_{Rd}^z \rangle \langle S_{R'd'}^z \rangle e^{i\mathbf{Q} \cdot (\mathbf{R} - \mathbf{R}' + \mathbf{d} - \mathbf{d}')} \delta(\hbar\omega)$$

Here $\gamma = 1.913$ is the ratio between the neutron dipole moment and the nuclear Bohr magneton, $r_0 = 2.8179$ fm is the classical electron radius, $|F(\mathbf{Q})|$ is the cerium form factor, \hat{Q}_z is the z -component of the unit scattering vector $\hat{\mathbf{Q}}$. The factor $1/N$ where N is the number of unit cells of volume v_N ensures consistent normalization with Eq. 4.

For simplicity, we assume that any magnetic order is uniaxial and polarized along the \mathbf{c} axis. Other assumptions will modify the inferred limits by factors of order unity.

For three-dimensional magnetic orders, we obtain

$$\left(\frac{d^2\sigma}{d\Omega dE_f}\right)_{\text{el}}^{\text{mag}} = \left(\frac{\gamma r_0}{2}\right)^2 |F(\mathbf{Q})|^2 (1 - \hat{Q}_z^2) (m_z/\mu_B)^2 \frac{(2\pi)^3 N_m}{v_m N} \sum_{\boldsymbol{\tau}_m} |\mathbb{F}_m(\boldsymbol{\tau}_m)|^2 \delta^3(\mathbf{Q} - \boldsymbol{\tau}_m) \delta(\hbar\omega) \quad (15)$$

Here N_m is the number of magnetic unit cells of volume v_m , $\boldsymbol{\tau}_m$ are reciprocal lattice vectors of the magnetic unit cell, m_z is the ordered magnetic dipole moment, and $\mathbb{F}_m(\mathbf{Q})$ is the scalar magnetic structure factor:

$$\mathbb{F}_m(\mathbf{Q}) = \sum_{\mathbf{d}_m} \exp(-i\mathbf{Q} \cdot \mathbf{d}_m). \quad (16)$$

Here \mathbf{d}_m indicates position vectors for magnetic ions within the magnetic unit cell and we have suppressed the Debye-Waller factor for simplicity. From the analogous forms of the magnetic and nuclear Bragg diffraction cross-section we readily obtain the following:

$$m_z^2 = \frac{\int_{\boldsymbol{\tau}_m} d^3\mathbf{Q} \hbar d\omega \mathcal{I}_m(\mathbf{Q}, \omega)}{\int_{\boldsymbol{\tau}} d^3\mathbf{Q} \hbar d\omega \mathcal{I}_N(\mathbf{Q}, \omega)} \cdot \frac{A(\boldsymbol{\tau}, 0)}{A(\boldsymbol{\tau}_m, 0)} \cdot \left(\frac{v_m}{v_N}\right)^2 \cdot \frac{|\mathbb{F}_N(\boldsymbol{\tau})|^2}{\left(\frac{\gamma r_0}{2}\right)^2 |F(\boldsymbol{\tau}_m)|^2 (1 - \hat{\tau}_{mz}^2) |\mathbb{F}_m(\boldsymbol{\tau}_m)|^2} \mu_B^2. \quad (17)$$

Here we have used $N_m v_m = N v_N$ and introduced the sample absorption correction. In Figure S3, we show the elastic scattering along the (hh) and $(h1)$ directions, from which we calculate $\int_{\boldsymbol{\tau}_m} d^3\mathbf{Q} \hbar d\omega \mathcal{I}_m(\mathbf{Q}, \omega)$ for putative magnetic orders at $(\frac{1}{2}\frac{1}{2})$ and (01) , respectively.

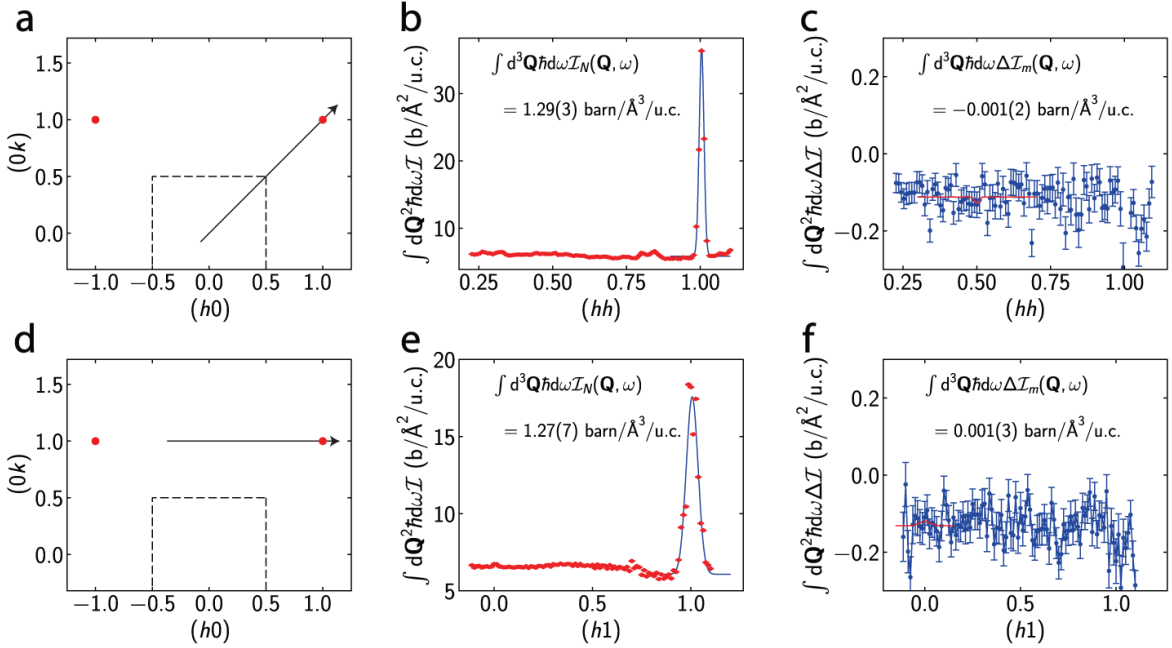


FIG. S3. (a) Schematic of the (hk) plane and the cut along the (hh) direction. (b) Elastic scattering along (hh) . Since no discernible difference was observed between 0.08 K and 0.8 K, data are averaged to enhance statistics. (c) Temperature difference (0.08 K - 0.8 K) of the elastic scattering along (hh) . Data in (b,c) are averaged along $(k\bar{k})$ and l in windows of ± 0.10 and ± 0.5 r.l.u., respectively. The energy window is from -0.2 meV to 0.2 meV. Gaussian peaks are fitting for the (110) nuclear peak (b) and putative magnetic scattering at $(\frac{1}{2}\frac{1}{2})$ (c). (d) Schematic of the (hk) plane and the cut along the $(h1)$ direction. (e) Elastic scattering along $(h1)$. 0.08 K and 0.8 K data are averaged. (f) Temperature difference (0.08 K - 0.8 K) of the elastic scattering along $(h1)$. Data in (e,f) are averaged along $(0k)$ and l in windows of ± 0.15 and ± 0.5 r.l.u., respectively. The energy window is from -0.2 meV to 0.2 meV. Gaussian peaks are fitted for the (110) nuclear peak (e) and putative magnetic scattering at (01) (f).

For quasi-two-dimensional magnetic order, there are no magnetic correlations between cerium planes and the diffraction cross-section takes this form

$$\left(\frac{d^2\sigma}{d\Omega dE_f}\right)_{\text{el}}^{\text{mag}} = \left(\frac{\gamma r_0}{2}\right)^2 |F(\mathbf{Q})|^2 (1 - \hat{Q}_z^2) (m_z/\mu_B)^2 \frac{(2\pi)^2}{A_m} \frac{N_m}{N} \sum_{\tau_m} |\mathbb{F}_m(\boldsymbol{\tau}_{\parallel m})|^2 \delta^2(\mathbf{Q}_{\parallel} - \boldsymbol{\tau}_{\parallel m}) \delta(\hbar\omega) \quad (18)$$

Here N_m is the number of 2D magnetic unit cells with area A_m and \mathbb{F}_m is the corresponding scalar magnetic structure factor. Note that $\frac{1}{2}N_m A_m c = N v_n$ where the factor of a half arises because there are two cerium layers per nuclear unit cell.

Since the CNCS instrument used in this work only covers a relatively small range of wave vector transfer perpendicular to the scattering plane, we can approximate the resolution function with a factorized form:

$$\mathcal{R}_{\mathbf{Q},\omega}(\delta\mathbf{Q}, \delta\omega) \approx \mathcal{R}_{\mathbf{Q}_{\parallel},\omega}^{\parallel}(\delta\mathbf{Q}_{\parallel}, \delta\omega) \mathcal{R}^{\perp}(\delta\mathbf{Q}_z), \quad (19)$$

where both \mathcal{R}^{\parallel} and \mathcal{R}^{\perp} are unity normalized over their domain. Convoluting Eq. 18 with this form of the resolution function, we obtain the following approximate form for the resolution smeared diffraction cross-section:

$$\left(\frac{d^2\sigma}{d\Omega dE_f}\right)_{\text{el}}^{\text{mag}} = \left(\frac{\gamma r_0}{2}\right)^2 |F(\mathbf{Q})|^2 (1 - \hat{Q}_z^2) (m_z/\mu_B)^2 \frac{(2\pi)^2}{A_m} \frac{N_m}{N} |\mathbb{F}_m(\boldsymbol{\tau}_{\parallel m})|^2 \mathcal{R}_{\mathbf{Q}_{\parallel},\omega}^{\parallel}(\mathbf{Q}_{\parallel} - \boldsymbol{\tau}_{\parallel m}, \omega) \quad (20)$$

This finally leads to an expression for the staggered magnetization:

$$m_z^2 = \frac{\int_{\tau_m} d^3\mathbf{Q} \hbar d\omega \mathcal{I}_m(\mathbf{Q}, \omega) (|F(\mathbf{Q})|^2 (1 - \hat{Q}_z^2))^{-1}}{\int_{\tau} d^3\mathbf{Q} \hbar d\omega \mathcal{I}_N(\mathbf{Q}, \omega)} \cdot \frac{A(\boldsymbol{\tau}, 0)}{A(\boldsymbol{\tau}_m, 0)} \cdot \left(\frac{A_m c}{v_N}\right)^2 \cdot \frac{(c^*/\Delta Q_z) |\mathbb{F}_N(\boldsymbol{\tau})|^2}{(\frac{\gamma r_0}{2})^2 2 |\mathbb{F}_m(\boldsymbol{\tau}_{\parallel m})|^2} \mu_B^2 \quad (21)$$

Here ΔQ_z is the range of integration along the \mathbf{c} direction for the \mathbf{Q} integration in the numerator and we have used $N_m/N = 2(v_N/A_m c)$. Table S1 shows the in-plane area of the magnetic unit cell A_m , the c -axis lattice parameter of the magnetic unit cell c_m , polarization factor $(1 - \hat{Q}_z^2)$, magnetic form factor $|F(\mathbf{Q})|$, $|\mathbb{F}_m|$, and corresponding m_z^2 and upper bounds for putative magnetic orders at specific wavevectors. Note that there are magnetic peaks at both $l = -0.5$ and 0.5 for $(\frac{1}{2}\frac{1}{2}\frac{1}{2})$ and $(01\frac{1}{2})$ order, but this factor is coincidentally compensated by the fact that the l coverage is -0.5 to 0.5 r.l.u.

TABLE S1. Magnetic ordering and upper limit of moment determined from the corresponding analysis of our diffraction data.

wavevector \mathbf{Q}	$A_N/A(\mathbf{Q}, \omega)$	A_m	c_m	$(1 - \hat{Q}_z^2)$	$ F(\mathbf{Q}) $	$ \mathbb{F}_m ^2$	$m_z^2(\mu_B^2)$	$m_{\parallel, \max} (\mu_B)$
$(\frac{1}{2}\frac{1}{2}0)$	2.46	4a	c	1	0.937	64	0.00(1)	0.10
$(\frac{1}{2}\frac{1}{2}\frac{1}{2})$	2.46	4a	2c	0.914	0.932	128	-0.01(3)	0.14
(010)	1.65	a	c	1	0.880	4	0.01(1)	0.14
$(01\frac{1}{2})$	1.65	a	2c	0.955	0.875	8	0.01(3)	0.22
quasi-2D $(\frac{1}{2}\frac{1}{2})$	2.46	4a	c	> 0.914	> 0.932	16	-0.01(3)	0.14

V. SCATTERING FROM CYTOP

We used the fluoropolymer-based adhesive CYTOP to attach the crystals. CYTOP has a powder-like diffraction peak around 1.1 Å, which practically coincides with $\mathbf{Q}_{\text{AF}} = (\frac{1}{2}\frac{1}{2})$ in CeRh_2As_2 , as shown in Figure S4(a). Therefore, it is crucial to examine whether the peak at \mathbf{Q}_{AF} could be from CYTOP. We can rule this out because scattering from CYTOP is approximately isotropic and independent of sample rotation while magnetic scattering is four-fold rotational symmetric.

To compare the scattering from CYTOP with the excitation spectrum, we scaled the (hh) cut of the CYTOP scattering to that of the peak at 0.3 meV and constructed the $(k\bar{k})$ and $(0k)$ cuts for CYTOP (Fig. S4(b,c)). The CYTOP scattering is wider than the observed excitations centered at $\mathbf{Q}_{\text{AF}} = (\frac{1}{2}\frac{1}{2})$ in the $(k\bar{k})$ cut. In addition, CYTOP also shows a peak in the $(0k)$ cut, which is absent in the measured spectrum.

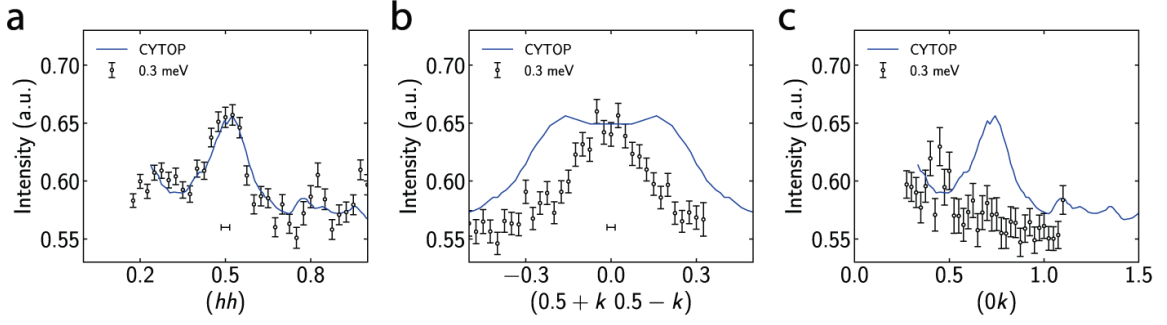


FIG. S4. (a) Constant energy cuts along the longitudinal (hh) direction at 0.3 meV. The averaging windows along $(k\bar{k})$ and l directions are ± 0.15 , and ± 0.5 r.l.u., respectively. (b) Constant energy cuts along the transverse ($k\bar{k}$) direction at 0.3 meV. The averaging windows along (hh) and l directions are ± 0.1 , and ± 0.5 r.l.u., respectively. (c) Constant energy cuts along the longitudinal k direction at 0.3 meV. The averaging windows along h and l directions are ± 0.2 , and ± 0.5 r.l.u., respectively. The energy window is ± 0.1 meV. The horizontal error bars represent the resolution width.

VI. NESTING FUNCTION

The nesting function was obtained from DFT calculations, yet it does not display a pronounced peak at $(\frac{1}{2}, \frac{1}{2})$ (Fig. S5(a)). This absence of a clear nesting feature is common in heavy-fermion superconductors. Such deviations from expected nesting peaks underscore the complex interplay of electronic structure and interactions in these materials, which may not be fully captured by standard DFT methods alone.

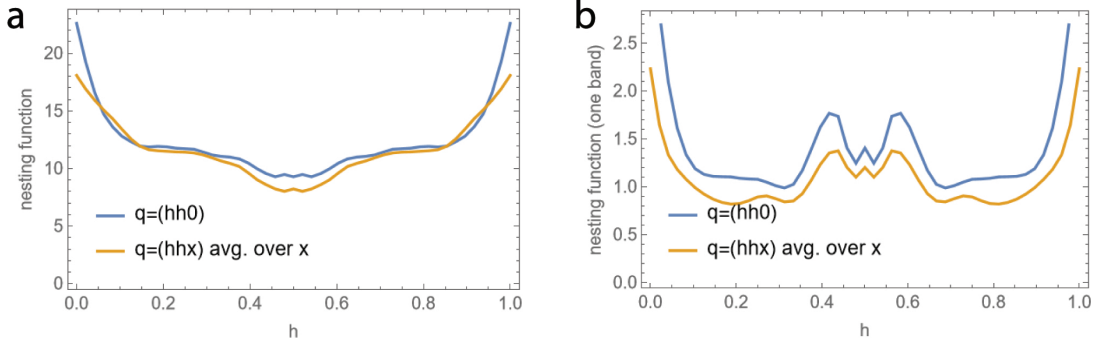


FIG. S5. (a) Wavevector dependence of nesting function from DFT calculations. (b) Wavevector dependence of nesting function for one band. Blue curves are calculated at $l = 0$ and orange curves are calculated with averaged l .

-
- [1] H. Siddiquee, Z. Rehfuss, C. Broyles, and S. Ran, Pressure dependence of superconductivity in CeRh_2As_2 , *Physical Review B* **108**, L020504 (2023).
 - [2] T. Hahn, U. Shmueli, and J. W. Arthur, *International tables for crystallography*, Vol. 1 (Reidel Dordrecht, 1983).
 - [3] O. Arnold, J.-C. Bilheux, J. Borreguero, A. Buts, S. I. Campbell, L. Chapon, M. Doucet, N. Draper, R. F. Leal, M. Gigg, *et al.*, Mantid—data analysis and visualization package for neutron scattering and μ sr experiments, *Nuclear Instruments and Methods in Physics Research Section A: Accelerators, Spectrometers, Detectors and Associated Equipment* **764**, 156 (2014).
 - [4] C. Dwiggins, Rapid calculation of x-ray absorption correction factors for cylinders to an accuracy of 0.1%, *Acta Crystallographica Section A: Crystal Physics, Diffraction, Theoretical and General Crystallography* **31**, 146 (1975).
 - [5] NIST center for neutron research tabulated neutron scattering lengths and cross sections, <https://www.ncnr.nist.gov/resources/n-lengths/list.html>.
 - [6] V. F. Sears, Neutron scattering lengths and cross sections, *Neutron News* **3**, 26 (1992).